Root-driven weathering impacts on mineral-organic associations in deep soils over pedogenic time scales

Mariela Garcia Arredondo [a], Corey R. Lawrence [b], Marjorie S. Schulz [c], Malak M. Tfaily [d], Ravi Kukkadapu [e], Morris E. Jones [a], Kristin Boye [f], Marco Keiluweit [a,*]

[a] *School of Earth & Sustainability and Stockbridge School of Agriculture, University of Massachusetts, Amherst, MA, USA*
[b] *U.S. Geological Survey, Geosciences and Environmental Change Science Center, Denver, CO, USA*
[c] *U.S. Geological Survey, Biogeochemistry of Soils Group, Menlo Park, CA, USA*
[d] *Soil, Water and Environmental Science Department, University of Arizona, Tucson, AZ, USA*
[e] *Environmental Molecular Sciences Lab, Pacific Northwest National Laboratory, Richland, WA, USA*
[f] *Stanford Synchrotron Radiation Lightsource (SSRL), Menlo Park, CA, USA*

Received 24 September 2018; accepted in revised form 15 July 2019; available online 23 July 2019

Abstract

Plant roots are critical weathering agents in deep soils, yet the impact of resulting mineral transformations on the vast deep soil carbon (C) reservoir are largely unknown. Root-driven weathering of primary minerals may cause the formation of reactive secondary minerals, which protect mineral-organic associations (MOAs) for centuries or millennia. Conversely, root-driven weathering may also transform secondary minerals, potentially enhancing the bioavailability of C previously protected in MOAs. Here we examined the impact of root-driven weathering on MOAs and their capacity to store C over pedogenic time scales. To accomplish this, we examined deep horizons (100–160 cm) that experienced root-driven weathering in four soils of increasing ages (65–226 kyr) of the Santa Cruz marine terrace chronosequence. Specifically, we compared discrete rhizosphere zones subject to root-driven weathering, with adjacent zones that experienced no root growth. Using a combination of radiocarbon, mass spectrometry, ^{57}Fe Mössbauer spectroscopy, high-resolution mass spectrometry, and X-ray spectromicroscopy approaches, we characterized transformations of MOAs in relation to changes in C content, Δ^{14}C values, and chemistry across the chronosequence. We found that the onset of root-driven weathering (65–90 kyr) increased the amount of C associated with poorly crystalline iron (Fe) and aluminum (Al) phases, particularly highly disordered nano-particulate goethite (np-goethite). This increase coincided with greater C concentrations, lower Δ^{14}C values, and greater abundance of what is likely microbially-derived C. Continued root-driven weathering (137–226 kyr) did not significantly change the amount of C associated with crystalline Fe and Al phases, but resulted in a decline in the amount of C associated with poorly crystalline Fe and Al phases. This decline coincided with a decrease in C concentrations, an increase in Δ^{14}C values, and a shift toward plant-derived C. In contrast, soil not affected by root-driven weathering showed comparatively low amounts of C bound to poorly crystalline Fe and Al phases regardless of soil age and, correspondingly, lower C concentrations. Our results demonstrate that root-driven formation and disruption of MOAs are direct controls on both C accrual and loss in deep soil.

* Corresponding author at: University of Massachusetts Amherst, 161 Holdsworth Way, Amherst, MA 01003, USA.
E-mail address: keiluweit@umass.edu (M. Keiluweit).

This finding suggests that root impacts on soil C storage are dependent on soil weathering stage, a consideration that is critical for future predictions of the vulnerability of deep soil C to global change.

Keywords: Rhizogenic weathering; Organo-mineral interactions; Soil organic matter; Mineral dissolution; Short-range order minerals; Metal-organic complexes; Sequential extractions

1. INTRODUCTION

Soils play a critical role in the global carbon (C) cycle because they contain 3300 Pg of C, which is more than twice the amount stored in the atmosphere (Jobbagy and Jackson, 2000; Tarnocai et al., 2009). More than half of total soil C stocks reside in soils > 1 m in depth (Harper and Tibbett, 2013), where C can be stored for millennia (Ewing et al., 2006). However, several studies have demonstrated a dramatic response of this deep soil C to environmental change (Bernal et al., 2016; Richter et al., 1999; Fontaine et al., 2007). Deep soil C appears to be particularly vulnerable to increased root growth as induced by elevated CO_2 (Kuzyakov, 2011), drying climates (Fan et al., 2017), or vegetation change (Richter et al., 1999; Bernal et al., 2017). To model and predict how deep soil C responds to such perturbations, a better understanding of the mechanisms controlling soil C storage at depth is needed.

Due to the greater abundance of reactive metal phases, mineral-organic associations (MOAs) are assumed to be the quantitatively most important C protection mechanism in deeper soils (Rumpel and Kögel-Knabner, 2011). Poorly crystalline iron (Fe), manganese (Mn) and aluminum (Al) (hydr)oxides, amorphous metal-organic complexes, and aluminosilicates have a high affinity for organic compounds due to their large surface areas and reactive bonding sites (Mikutta et al., 2009). The resulting MOAs often dramatically reduce microbial and enzymatic access to organic C (Kleber et al., 2015), thereby protecting C from loss processes for millennia (Torn et al., 1997). However, MOAs are subject to weathering during soil development (Chadwick and Chorover, 2001; Chorover et al., 2004), altering the crystallinity of mineral phases (Thompson et al., 2006) and their ability to protect C (Torn et al., 1997; Mikutta et al., 2009). While these studies significantly advanced our understanding of weathering influences on MOAs over pedogenic time scales, the influence of root-driven weathering reactions has been largely ignored.

Roots release 40–60% of photosynthetically fixed C into the soil as sloughed-off root cells and tissues, mucilage and exudates (Heinemeyer et al., 2007), with root-derived and root-associated microbial C contributing up to 50–70% of total soil C stocks (Clemmensen et al., 2013). The release of such organic compounds reshapes the rhizosphere, which we herein define as a zone under direct physical, chemical and biological influence of roots (Richter et al., 2007), altering geochemical and microbial processes to promote mineral weathering (Fimmen et al., 2008; Schulz et al., 2016). Organic acids, reductants, and metal chelators released by roots and associated microbes can directly dissolve minerals (Richter et al., 2007; Hinsinger and Courchesne, 2008). Further, roots release protons and CO_2, acidifying the soil and increasing the solubility of secondary minerals (April and Keller, 1990) which serve as building blocks for MOAs. Moreover, oxygen consumption by roots and microbes is often strong enough to create reducing conditions in the rhizosphere (Husson, 2013), which promotes reductive dissolution of secondary Fe (hydr)oxides (Fischer et al., 1989; Fimmen et al., 2008). Yet, to date, studies focusing on the development and C storage potential of MOAs (Torn et al., 1997; Chorover et al., 2004; Mikutta et al., 2009) have largely overlooked the potential impacts of such root-driven weathering reactions.

This is particularly true of deep soils, where weathering is generally perceived as driven by abiotic processes (Moore et al., 2010; Lawrence et al., 2015), even though biotic processes induced by root systems can extend to depths far beyond 1 m (Oh and Richter, 2005; Richter et al., 2007). Rooting depths are controlled by lithologic, climatic and hydrologic factors and can reach depths of >70 m (Schenk and Jackson, 2002; Fan et al., 2017). Roots extending into the bedrock, along with associated microbes, are increasingly recognized as principal weathering agents (Leake et al., 2008), promoting the transformation of primary into secondary minerals (Brantley et al., 2011). Rhizosphere soil can thus be enriched in secondary phases, such as poorly crystalline Fe and Al (hydr)oxides (April and Keller, 1990; Séguin et al., 2005). Recently, Schulz et al. (2016) compared deep soil that had experienced root-driven weathering with soil of the same age that remained unaffected by roots. It was shown that root-driven weathering created poorly crystalline Fe and Al phases, which are known to have a strong effect on C storage (Masiello et al., 2004; Lawrence et al., 2015). Another study suggested that root exudate-mediated weathering of primary minerals produces crystalline Fe and Al phases that act as templates for the formation of MOAs (Yu et al., 2017), suggesting that root-driven weathering is essential for the protection of C in MOAs.

However, root-driven weathering may not only form MOAs, it can also transform and dissolve secondary mineral phases. Seasonal variations in root activity have been shown to transform secondary minerals by dissolving Fe and Al (hydr)oxides (Collignon et al., 2012), or hydroxylating clay mineral surfaces and interlayers (Augusto et al., 2001; Turpault et al., 2007). Observations of root-driven weathering over longer time scales by Fimmen et al. (2008) found that roots promote solubilization and re-precipitation of Fe away from the root, causing the relative enrichment of Al hydroxides in the near-root environment (i.e., rhizosphere soil). Dissolution and/or transformations

of secondary minerals may directly affect reactive surface sites and their capacity to bind organic compounds (Chorover et al., 2004; Thompson et al., 2006). In fact, a recent study by Keiluweit et al. (2015) demonstrated that selected root exudates can disrupt MOAs, solubilizing previously mineral-bound organic C and making it more susceptible to microbial conversion to CO_2. The notion that roots can disrupt MOAs is further supported by the significant loss of old C protected in deep soils (Fontaine et al., 2007; Bernal et al., 2016) and associated with poorly crystalline Fe and Al phases (Rasmussen et al., 2007; Finley et al., 2018) in response to the addition of root-derived organic compounds. Combined, these studies suggest that root-driven weathering may not only promote the formation, but also the disruption of MOAs, with unclear consequences for soil C storage.

The main objective of this study was to determine the impact of root-driven weathering on MOAs and soil C over pedogenic time scales. To accomplish our objective, we examined MOA transformations in relation to C dynamics in deep soil horizons of the Santa Cruz marine terraces chronosequence (White et al., 2008; Schulz et al., 2016). Soil development and weathering in this chronosequence has been extensively studied using measurements (White et al., 2008, 2009, 2012) and reactive transport models (Maher et al., 2009; Lawrence et al., 2014). Deep soil horizons at this site are particularly suited for this study because they feature discrete zones created by root-driven weathering (here termed "rhizosphere soil"). Schulz et al. (2016) established that the formation of this rhizosphere soil is an effect of initial colonization and repeated growth of deep roots into pores or fractures, possibly created by shrink/swell behavior (White and Kirkegaard, 2010). Preferential growth of new roots and root decay into the same soil spaces created a weathering regime that–over pedogenic timescales–caused the formation of mineralogically distinct rhizosphere soil (see photographs in Schulz et al., 2016). In contrast, adjacent soil zones did not experience root growth and were not subjected to direct root-driven weathering. In the absence of roots, this "non-rhizosphere soil" experienced a different weathering regime and, thus, developed mineralogical characteristics distinct from those of rhizosphere soil. This non-rhizosphere soil may have been influenced by solute exchange with the rhizosphere soil, but direct weathering impact of roots can be considered negligible (Schulz et al., 2016). Here, we expand on this work and related efforts by directly addressing the question of how root-driven weathering affected MOA dynamics and how those, in turn, affected C storage over pedogenic timescales.

To follow the impact of root-driven weathering over time, we analyzed samples from four soil profiles ranging in age from 65 to 226 kyr across the chronosequence, and directly compared rhizosphere to non-rhizosphere soil in each profile. Sample characterization was guided by three objectives: to determine the effects of root-driven weathering on (i) C concentration, $\Delta^{14}C$ values and C chemistry, (ii) mineralogical composition, particularly changes in poorly crystalline Fe and Al phases, and (iii) the degree of association between C and Fe or Al phases at the micron-scale. To this end, we used a suite of solid-phase analyses, including radiocarbon measurements, high-resolution Fourier-transform ion cyclotron mass spectrometry (FT-ICR-MS), quantitative sequential extractions, Mössbauer spectroscopy, and scanning transmission X-ray microscopy (STXM). Our results indicate a strong coupling between root-driven MOAs transformations and soil C accrual or loss over pedogenic timescales.

2. MATERIALS AND METHODS

2.1. Site description

The marine terrace soil chronosequence is located in coastal California just north of Santa Cruz, CA, USA, and consists of five spatially distinct coastal terraces ranging in age from 65 kyr to 226 kyr (White et al., 2008). The terraces increase in age and elevation with distance from the modern coastline (Schulz et al., 2018). The soils developed on the marine terraces are generally classified as Mollisols and have developed from shallow marine sediment deposits (Schulz et al., 2018). Terrace deposits are predominantly composed of granodiorite to quartz diorite, with some amounts of gabbro, sandstone and mudstone (White et al., 2008). The mudstone contains little clay and ranges from a siliceous, organic-rich mudstone to a porcelanite (El-Sabbagh and Garrison, 1990). The Santa Cruz marine terrace chronosequence has been dated using ^{10}Be and ^{26}Al (Perg et al., 2001). The age determination has facilitated quantitative testing and development of reactive transport models for weathering and soil-profile development (Maher et al., 2009; Lawrence et al., 2014). The predominant vegetation is open coastal prairie (combination of native and European grasses) interspersed with California oak woodlands. The current climate is Mediterranean, with cool wet winters and warm dry summers with mean annual precipitation and temperature of ~730 mm and 13.4 ° C (Schulz et al., 2016). Terraces 1, 2, 3, and 5 of the Santa Cruz marine chronosequence are 65, 90, 137, and 226 kyr respectively. The youngest soil (65 kyr, terrace 1) has an A horizon but no Bt horizon and, while indirect root influences cannot be excluded, no evidence of rhizosphere development at depths greater than 1 m is currently observed for this terrace. In this soil, orange-hued Fe oxides have formed a relatively uniform coating on primary mineral grains throughout the sediment deposit. Older members of the Santa Cruz marine terrace chronosequence (90–226 kyr, terraces 2–5) display Bt horizons at depths > 1 m with roots found at depths > 1 m. These Bt horizons feature vertical, gray, low-chroma weathering zones subjected to root activity (rhizosphere soil) surrounded by orange, high-chroma zones that did not experience root growth and are similar to the Fe oxide rich subsoils in terrace 1 (non-rhizosphere soil) (Schulz et al., 2016). These distinct color (and mineralogical) differences between rhizosphere and non-rhizosphere soil are comparable to those observed by Fimmen et al. (2008) in humid forested ecosystems.

2.2. Soil sampling

Soil samples from terraces 1–3 and 5 were collected using a hand-auger from depths showing the most pronounced rhizosphere differentiation (depths = 120–170 cm). Triplicate cores were taken on each terrace at random locations. In the lab, rhizosphere soil was carefully separated from non-rhizosphere soil for terraces 2, 3 and 5, based on the color differences described above, and dried in the dark in an anaerobic chamber to prevent transformations of Fe and redox active metals. All soil from terrace 1 was considered as non-rhizosphere soil due to the absence of visible rhizogenic weathering zones. Terrace 4 was not sampled because it is known to have been subjected to recent anthropogenic disturbance where the top 30 cm had been removed (White et al., 2008). Chemical analyses were performed on each biological replicate except for those with very low throughput and high analytical cost (radiocarbon, Mössbauer, FT-ICR-MS, and X-ray spectromicroscopy). Here, equal amounts (on a mass basis) of three biological replicates for rhizosphere and non-rhizosphere soil at each terrace were pooled into one composite sample that was analyzed.

2.3. Total carbon

To determine total C concentration, samples were analyzed via an ECS 4010 CHNS-O elemental analyzer (Costech Analytical Technologies, Inc., Valencia, CA, USA), with acetanilide as our standard. These C analyses were performed on all samples (triplicate cores from each terrace separated into rhizosphere and non-rhizosphere soil). Since our soils have relatively low pH our soils are considered free of inorganic C, as confirmed by the lack of carbonates in our X-ray diffraction (XRD) data and other studies (Moore et al., 2010).

2.4. Radiocarbon analysis

Composite samples from each zone and terrace were submitted to the University of California, Irvine W.M. KECK Carbon Cycle Accelerator Mass Spectrometry Laboratory (UCI-KECK AMS), where sample carbon was converted to CO_2 through combustion with CuO at 900 °C. The CO_2 was then cryogenically extracted and purified on a vacuum line and yield was measured using pressure change in a known volume (Xu et al., 2007). Approximately 1 mg of CO_2 was partitioned into a glass tube containing Zi + TiH_2 catalyst filament and sealed with a torch prior to graphitization in a furnace for 500–550 °C for 7 h. Any remaining CO_2 was retained for $\delta^{13}C$ measurement by isotope ratio mass spectrometry (IRMS). After graphitization, graphite was packed into a 1 mm diameter aluminum target and loaded on the UCI-KECK AMS for ^{14}C measurement. The ^{14}C abundance was normalized to a constant $\delta^{13}C$ using AMS measurements for both values, allowing for correction of natural isotope fractionation as well as any fractionation that occurs within the AMS system (Xu et al., 2007).

2.5. Quantitative X-ray diffraction

Composite samples were prepared for XRD using a modified method based on Eberl (2003). One gram of homogenized sample was mixed with 20% corundum and ground in a McCrone micronizing mill with 4 mL ethanol for 5 min, generating particle sizes on the order of 10–30 μm. After drying at 60 °C, the mixture was transferred to a plastic scintillation vial with three delrin balls (~1 cm in diameter) along with 200–800 μL Vertrel® solution (Dupont) and shaken for 10 min. The powder was passed through a 250-μm sieve to break up larger aggregates and loaded onto an XRD sample holder. Samples were analyzed using a Siemens D500 X-ray diffractometer from 5 to 65 degrees two theta using Cu Kα X-ray radiation, with a step size of 0.02 degrees and a dwell time of 2 seconds per step. Quantitative mineral composition was calculated using the U.S. Geological Survey software, RockJock (Eberl, 2003), which fits XRD intensities of individual mineral standards to the measured diffraction pattern.

2.6. Sequential extractions

To determine the amount of poorly crystalline and crystalline material present in these soil samples, sequential wet-chemical extractions were performed on samples from terrace 1, as well as rhizosphere and non-rhizosphere soil from terraces 2, 3 and 5. Triplicates were hand-ground with mortar and pestle and 300 mg of each sample was weighed into 15 ml centrifuge tubes. Our sequential extraction followed the procedure developed by Heckman et al. (2018), which avoids C-based extractants to allow for the quantification of metal phases as well as the organic C compounds associated with them. The sequential extraction consisted of ultrapure H_2O to extract dissolved metals, pyrophosphate to solubilize metal-organic complexes (Ross and Wang, 1993), hydroxylamine to extract easily reducible phases (Ross and Wang, 1993), and dithionite to quantify total reducible metal phases (Wagai and Mayer, 2007). In each step, tubes received 10 ml of initial extractant, and the soil was suspended by briefly placing the mixture on a vortexer (30 s). The tubes were then placed on a shaker for 16 h (at 300 rpm), subsequently centrifuged (4000 × g) for 1 hr for pyrophosphate and 20 min for all other extractants. In between each extraction step, the remaining soil pellet was washed with 7 ml of ultrapure H_2O to remove excess extractant. Samples re-suspended in H_2O were placed on a shaker for 2 h and centrifuged at 4000 × g for 20 min. The supernatant was then combined with the previously recovered extract. The extract was filtered through 0.2-μm syringe filters and stored in the dark for further analysis. Aliquots were diluted, acidified with 2% nitric acid, and analyzed by ICP-MS (Shimadzu ICPMS-2030, Shimadzu Scientific Inst., Columbia, MD, USA) to determine Fe, Al and Si concentrations and separate aliquots were diluted and analyzed by total organic carbon analyzer (Shimadzu TOC-L CPH with an ASI-L, Shimadzu Scientific Inst., Columbia, MD, USA) to determine dissolved organic C concentrations in the extracts.

2.7. Fourier-transform ion cyclotron resonance mass spectrometry (FT-ICR-MS) analysis

A 12 Tesla Bruker SolariX FTICR spectrometer located at Environmental Molecular Science Lab–a DOE-BER national user facility located in Richland, WA–was used to obtain molecular information on the organic compounds in composites of water extracts. Other attempts to characterize the composition of the bulk and mineral-associated organic matter based on X-ray absorption spectroscopy and nuclear magnetic resonance spectroscopy failed due to the low C concentrations in our subsoils. The FT-ICR-MS analyses were focused on water extracts because water has been shown to extract the most diverse pool of organic compounds (Tfaily et al., 2015). Equal aliquots from triplicate water extracts (see sequential extraction above) were combined into a composite sample for analysis. Samples were then introduced into a standard Bruker ESI source to generate negatively charged molecular ions. The instrument was externally calibrated weekly to a mass accuracy of <0.1 ppm using a tuning solution from Agilent, which contains the following compounds: $C_2F_3O_2$, $C_6HF_9N_3O$, $C_{12}HF_{21}N_3O$, $C_{20}H_{18}F_{27}N_3O_8P_3$, and $C_{26}H_{18}F_{39}N_3O_8P_3$ with m/z ranging between 112 to 1333. The instrument settings were optimized by tuning on a Suwannee River Fulvic Acid standard. Blanks (HPLC grade MeOH) were also run at the beginning and the end of the day to monitor potential carry over from one sample to another. The instrument was flushed between samples using a mixture of water and methanol. The ion accumulation time (IAT) was varied between 0.1 and 0.3 s to account for differences in C concentration between samples. Ninety-six individual scans were averaged for each sample and internally calibrated using organic matter (OM) homologous series separated by 14 Da ($–CH_2$ groups). The mass measurement error was less than 1 ppm for singly charged ions across a broad m/z range (i.e. $200 < m/z < 1200$). To further reduce cumulative errors, all sample peak lists for the entire dataset were aligned to each other prior to formula assignment to eliminate possible mass shifts that would impact formula assignment. Putative chemical formulas were assigned using Formularity software made using Visual Studio (Microsoft Corporation) (Tolić et al., 2017). Chemical formulas were assigned based on the following criteria: S/N > 7, and mass measurement error < 1 ppm, taking into consideration the presence of C, H, O, N, S and P and excluding other elements. Peaks with large mass ratios (m/z values > 500 Da) often have multiple possible candidate formulas. These peaks were assigned formulas through propagation of CH_2, O, and H_2 homologous series. If multiple formula candidates were found, we consistently picked the formula with the lowest error and lowest number of heteroatoms, and the assignment of one phosphorus atom required the presence of at least four oxygen atoms. In this study, the number of C, H, O were set to be unlimited whereas N was set to be <=3, and P<=4. Peaks that were present in the blanks were subtracted from the sample data sets. Additionally, peaks that appeared in only one sample among all the samples (n = 16) were removed and not included in the downstream analysis. We identified 28,773 peaks among which more than half occurred only once, half of which were not assigned any molecular formula. Of the ones that were assigned molecular formula, the majority (90%) contained heteroatoms with very low intensities. On average, $4{,}427 \pm 428$ formula were identified in each sample. To emphasize differences between samples, we further eliminated those formula that are common among all samples (~266 peaks). The remaining "unique" formula amounted to on average $1{,}523 \pm 622$ per sample. To elucidate changes in the relative abundance of different compound classes, unique formulas were plotted on a van Krevelen diagram corresponding to their H/C versus O/C ratios (Kim et al., 2003) (Fig. EA-1). Using the H/C and O/C thresholds defined in Tfaily et al. (2015), compounds were broadly categorized as lipid, protein, lignin, tannin, carbohydrate, amino sugar, and unsaturated hydrocarbon-like compounds and their abundance was reported as number-averaged relative abundance. Number-averaged density plots of the number of oxygen atoms were evaluated as well, but no significant trends were observed (Fig. EA-2).

2.8. ^{57}Fe Mössbauer spectroscopy

Mössbauer spectra were collected at room temperature (RT), 140 K, 77 K, and 8 K using a Web Research Company (St. Paul, MN) instrument that included a closed-cycle cryostat SHI-850 obtained from Janis Research Company, Inc (Wilmington, MA), a Sumitomo CKW-21 He compressor unit, and a Ritverc (St. Petersburg, Russia) NaI detection system. ^{57}Co/Rh source (75-mCi, initial strength) was used as the gamma energy source. The raw data was folded to 512 channels to provide a flat background and a zero-velocity position corresponding to the center shift (CS) of a metal Fe foil at RT. Calibration spectra were obtained with a 7-μm-thick Fe foil (Amersham, England) placed in the same position as the samples to minimize any geometry errors. The Mössbauer data were modeled with Recoil software (University of Ottawa, Canada) using a Voigt-based structural fitting routine (Rancourt and Ping, 1991). Sample preparation and sample holder were identical to the procedures reported in Peretyazhko et al. (2013).

2.9. Scanning transmission X-ray microscopy (STXM) imaging

Scanning transmission X-ray microscopy (STXM) analyses were conducted at beamline SM 10ID-1 of the Canadian Lights Source (CLS) in Saskatoon, Canada. Composite soil samples were suspended in ultrapure H_2O (1:10 soil:solution ratio) and an aliquot of 1 μl was drop deposited on Si_3N_4 windows (Silson) and dried under vacuum. The sample chamber for STXM image collection was He-filled to minimize attenuation of the soft X-rays. Images were collected from three replicate regions of interest (25×25 μm^2) on the same window containing representative collections of particles for all samples. Each image included > 10 discernible particles. Images were collected at energies below and above the C K-edge (280 eV and 288.5 eV), 313 Fe L-edge (700 eV and 709.5 eV), and Al

K-edge (1560 eV and 1568 eV), respectively. Images were recorded with dwell times of 1 (C and Fe) or 3 ms (Al) and a pixel size of $40 \times 40\ nm^2$. Elemental maps for C, Fe and Al were generated by subtracting the aligned pre-edge image from the post-edge image using aXis2000 (McMaster University, Hamilton, Ontario, Canada). The spatial relationship between C, Fe and Al in each region of interest were further analyzed in the open-source image processing software Fiji (Schindelin et al., 2012; Rueden et al., 2017). To determine the spatial correlation of C with either Fe or Al, the Coloc2 plugin (Abramoff et al., 2004) was used to determine the Spearman's rank correlation coefficient. To quantify the degree of association between C and Fe or Al, a co-localization analysis was performed using the Colocalization Threshold plugin (Abramoff et al., 2004). The underlying algorithm calculates the number of pixels in which significant absorption of both C and Fe (or Al) is measured, relative to the total number of pixels in which significant absorption of only C is measured. The resulting values (expressed in percent) is a measure of the proportion of the total C in each image that is co-localized with Fe or Al. Correlation and co-localization analyses were performed for both C-Fe and C-Al pairs, but only the C-Fe pair is reported here. Because the Al K-edge is at significantly higher energy than the C K-edge and Fe L-edge, the spatial resolution and sensitivity for Al was insufficient for our quantitative imaging analysis.

2.10. Statistical analyses

One-way Analyses of Variance (ANOVA) were conducted using OriginPro2018 by Origin Lab followed by Fisher's least significant difference (LSD) pairwise comparison tests with the significance level set at $p < 0.05$. For synchrotron imaging Spearman's Rank Correlation analyses and Colocalization analyses were conducted in Fiji and the results were further compared using Fisher's LSD in OriginPro2018 with the significance level also set at $p < 0.05$.

3. RESULTS

3.1. Elemental and radiocarbon analyses

Elemental and radiocarbon analysis revealed consistently greater C concentrations (Fig. 1a, Table EA-1) and $\Delta^{14}C$ values (Fig. 1b) in rhizosphere than non-rhizosphere soil across the chronosequence. Relative to bulk soil from terrace 1, C concentrations in terrace 2 decreased significantly by approx. 50% ($p < 0.05$, Fisher's LSD) in non-rhizosphere soil. However, in rhizosphere soil in terrace 2, C concentrations were significantly increased by more than 30% ($p < 0.05$, Fisher's LSD). Between terraces 2 and 5, C significantly decreased by about 43% in rhizosphere soil ($p < 0.01$, Fisher's LSD). Contrastingly, C steadily decreased by over 67% in the non-rhizosphere soil from terrace 1 to 5 ($p < 0.01$, Fisher's LSD). Terrace 2 showed substantially more depleted $\Delta^{14}C$ values in both rhizosphere and non-rhizosphere soil than in the other terraces.

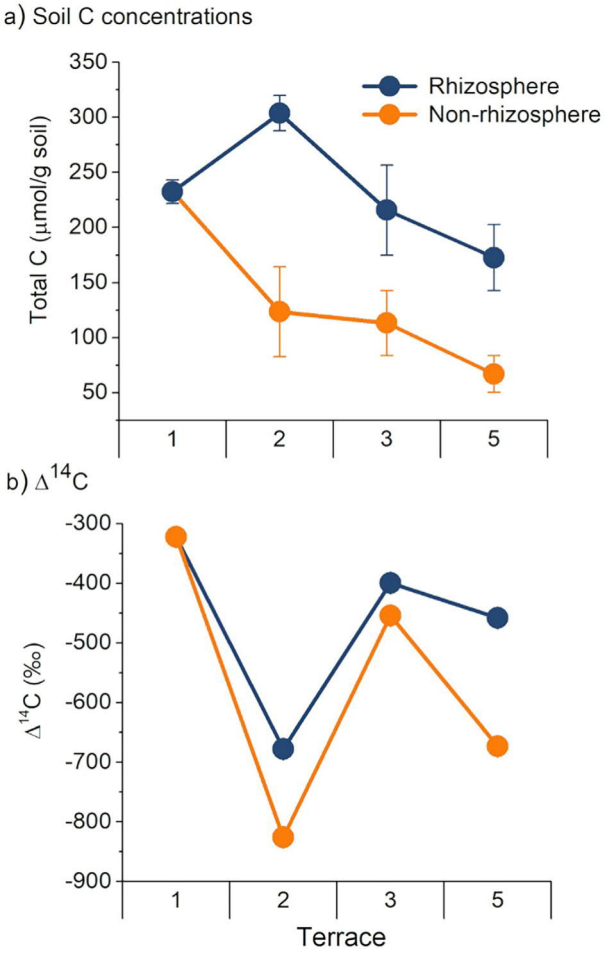

Fig. 1. Changes in (a) C concentration and (b) $\Delta^{14}C$ values in rhizosphere and non-rhizosphere soil across the chronosequence at depths greater than 1 m. Bars represent standard error of the mean of three replicate samples. Note that rhizosphere soil has not been established in terrace 1 and, thus, only data for bulk (i.e., non-rhizosphere soil) is shown.

3.2. Mineralogical composition

3.2.1. X-ray diffraction

The impact of root-driven weathering on the relative abundance of secondary minerals, particularly the formation and presence of phyllosilicate clays, was evaluated using XRD. Fitting of diffractograms showed that phyllosilicate clays in non-rhizosphere soils constituted approximately 30% of all XRD-detectable phases, and only increased at terrace 5 (Table EA-2). However, for rhizosphere soils the phyllosilicate clay portion more than doubled between terraces 1 and 2 to exceed 60%, and further increased to more than 70% in terraces 3 and 5. Conversely, the contributions from primary minerals diminished with soil age in rhizosphere soil. These observed trends indicate that phyllosilicate clays formed during the initial stages of root-driven weathering (65–90 kyr).

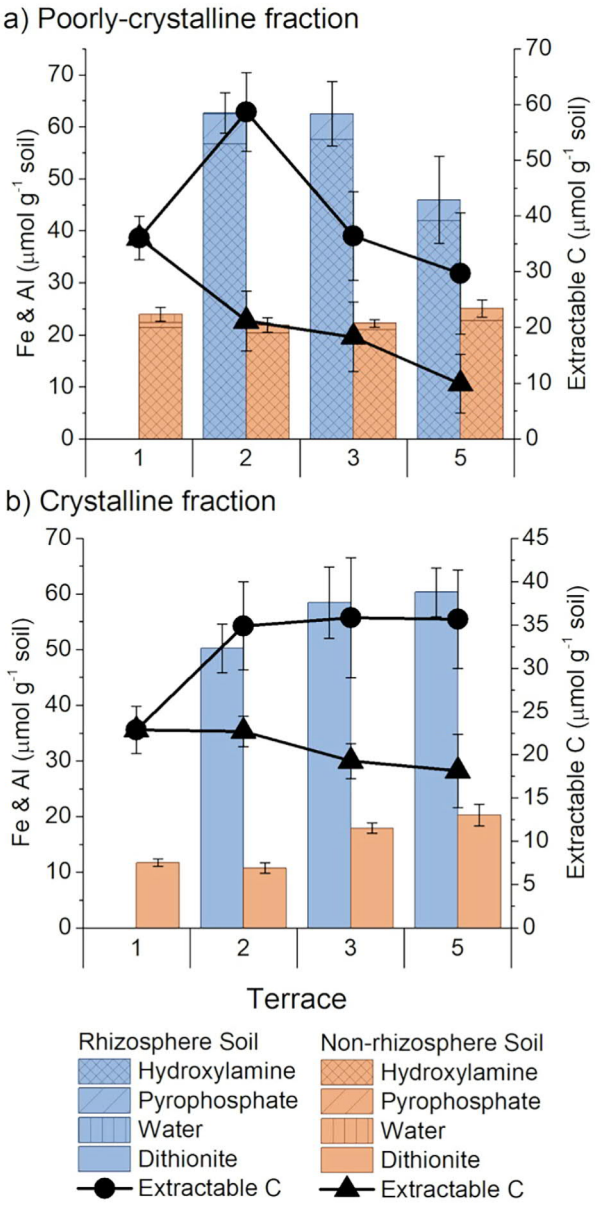

Fig. 2. Changes in extractable Fe and Al for (a) poorly crystalline and (b) crystalline phases, as well as C co-extracted with each phase, in non-rhizosphere and rhizosphere soil across the chronosequence. Poorly crystalline phases are presented as metals (Fe + Al) and C extracted by water, pyrophosphate and hydroxylamine, crystalline phases are metals (Fe + Al) and C released by dithionite. Bars represent standard error of the mean of three replicate samples. Note that rhizosphere soil has not been established in terrace 1 and, thus, only data for bulk (i.e., non-rhizosphere soil) is reported.

3.2.2. Sequential extractions

Sequential extractions were used to determine the impact of root-driven weathering on the relative abundance of poorly crystalline and crystalline Fe and Al phases, as well as the amount of organic C released upon extraction (Fig. 2). Extractable Fe and Al concentrations are within the range found by Schulz et al. (2016), but markedly lower than in subsoils examined in comparable studies (Lawrence et al., 2015; Fimmen et al., 2008). The amount of water, pyrophosphate, and hydroxylamine extractable Fe and Al (here defined as poorly crystalline phases) in non-rhizosphere soil remained relatively stable and was significantly lower than in rhizosphere soil across the chronosequence ($p < 0.05$, Fisher's LSD) (Fig. 2a). In contrast, the abundance of poorly crystalline Fe and Al phases increased significantly between terraces 1 and 2 in rhizosphere soil and significantly declined between terrace 3 and 5 ($p < 0.01$, Fisher's LSD). The extraction of greater amounts of poorly crystalline Fe and Al phases in rhizosphere soil coincided with a significantly larger mobilization of C when compared to non-rhizosphere soil ($p < 0.01$, Fisher's LSD) (Fig. 2a).

The amount of dithionite-extractable Fe and Al (here defined as crystalline phases) was significantly lower in non-rhizosphere soil compared to rhizosphere soil ($p < 0.01$, Fisher's LSD) (Fig. 2b). Morerover, the trends for crystalline Fe and Al phases differ from those observed for poorly crystalline phases. The amount of crystalline Fe and Al phases in non-rhizosphere soil, as well as the amount of associated C, did not change significantly with soil age ($p < 0.05$, Fisher's LSD). In contrast, crystalline Fe and Al phases in rhizosphere soil initially increased 4-fold from terrace 1 to 2 and plateaued thereafter. The amount of C associated with these crystalline phases in rhizosphere soil followed the same pattern – an initial increase by 75% in terrace 2, and unchanged values in terrace 3 and 5. The observed dynamics in rhizosphere soil indicate that initial root-driven weathering created poorly crystalline Fe and Al phases. However, more crystalline Fe and Al phases began to dominate the rhizosphere with continued weathering.

3.2.3. Mössbauer spectroscopy

Mössbauer spectra were obtained at room temperature (RT), 140, 77 and 8 K to gain insights into type and nature of Fe oxides in terms of their particle size, extent of metal or C substitution (Peretyazhko et al., 2013; Chen et al., 2017). The complete Mössbauer data, as well as a detailed discussion of fitting procedures and spectral interpretation, can be found in the EA (Figs. EA-3-9 and Tables EA-3-5).

Mössbauer spectra of rhizosphere and non-rhizosphere soils showed no evidence of ferrihydrite-like phases (Kaplan et al., 2016) or Fe(III)-organic matter complexes (Jung et al., 2012). In non-rhizosphere soil, Mössbauer spectra showed precipitation of ~90% of the total Fe as nano-particulate goethite (np-goethite, < 10 nm particle size, Table EA-3) (Cook et al., 1999; Bhattacharyya et al., 2018) with the remaining Fe (~10%) found in clay minerals. Furthermore, modeling suggested that np-goethite phases consist of three different general pools (or broad classes) labeled as type 1, type 2, and type 3. These differences were attributed to variations in particle size, which is a function of metal (Al) substitution (goethite with Al/(Al + Fe) ratio 0.16 display doublet at RT) (Fysh and Clark, 1982a, 1982b), with disorder increasing in the following order: type 1 > type 2 > type 3. The relative distribution (and, thus, the degree of disorder) of np-goethite phases in the rhizosphere

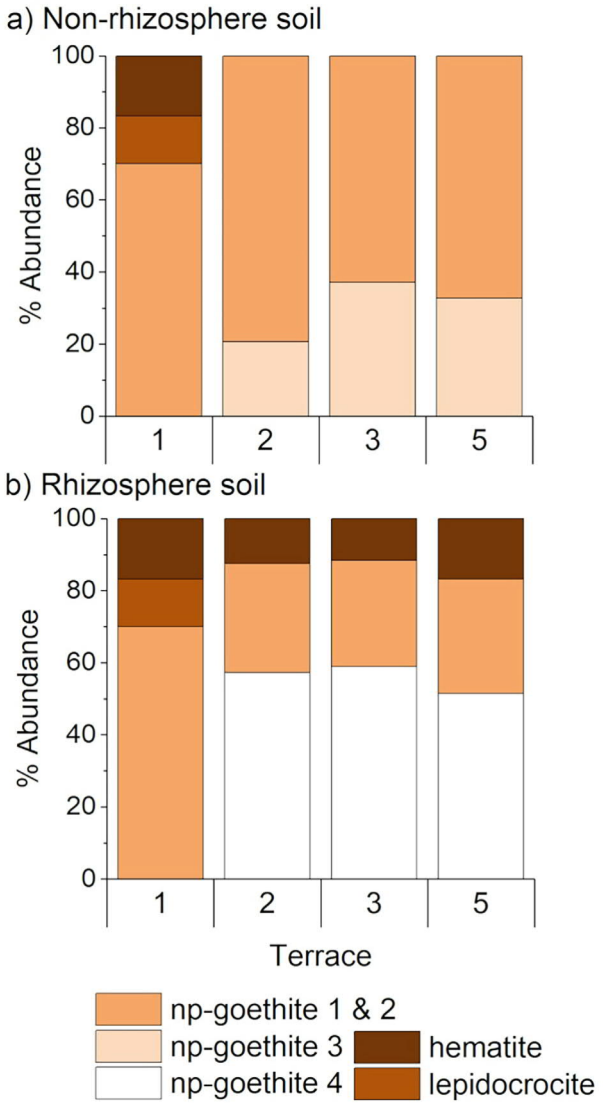

Fig. 3. Changes in abundance of Fe oxides of varying degree of disorder relative to total Fe oxides not including Fe in clays in (a) non-rhizosphere and (b) rhizosphere soil across the chronosequence as determined by ^{57}Fe Mössbauer spectroscopy. "np" = nano particulate. Note that rhizosphere soil has not been established in terrace 1 and, thus, data for bulk (i.e., non-rhizosphere soil) is shown in both panels.

soil are distinctly different from that in non-rhizosphere soils. For example, type 3 is absent, and a significant pool of a highly disordered np-goethite-type 4, with the lowest particle size and highest degree of metal substitution evident.

Rhizosphere and non-rhizosphere soil showed divergent trends in the np-goethite contributions in relation to total Fe-oxides present in these samples with increasing soil age (Fig. 3). The Fe oxide composition in terrace 1 was dominated by relatively ordered np-goethite phases (types 1 and 2), and minor contributions of lepidocrocite and np/Al-hematite. In terrace 2, however, distinct differences in Fe oxide mineralogy emerged between non-rhizosphere and rhizosphere soil. Both relatively more disordered np-goethite (type 3) and ordered np-goethite (types 1 and 2) dominated Fe oxide composition in non-rhizosphere soil (Fig. 3a). Their relative contributions (~20–36% and ~80–64%, respectively) remained constant from terrace 2 to 5. However, rhizosphere soil in terrace 2 did not show evidence for np-goethite (type 3). Instead, a highly disordered np-goethite (type 4) emerged in the rhizosphere soil (Fig. 3b and Supplemental Fig. EA-6, 7 and Table EA-4). This np-goethite (type 4) phase represented 58% of the Fe oxides detected in terrace 2, and its contribution steadily declined to ~50% between terrace 3 and 5. Our Mössbauer spectroscopy results indicate that these initial stages of root-driven weathering (terrace 2) promoted the formation of highly disordered np-goethite phases (type 4), the contribution of which declined with continued weathering (terrace 3–5).

3.3. Organic matter composition

3.3.1. Mass spectrometry

To determine the impact of root weathering on the composition of organic matter, we analyzed water extracts by high-resolution FT-ICR-MS (Fig. 4, Supplemental Figs. EA-1 and EA-2). In terrace 1, over 80% of the unique masses can be categorized as tannin, lignin, and carbohydrate-like compounds, while the remaining 20% of these unique masses were categorized as lipid, protein, amino sugar, and condensed hydrocarbon-like compounds (Fig. 4). With increasing soil age, non-rhizosphere soil showed a steady decline in tannin, lignin, and carbohydrate-like compound contribution relative to terrace 1. This decline was concurrent with proportional increases in the abundance of protein, lipid and amino sugar-like, which were the most dominant compound classes (>60% of total) in terrace 5 (Fig. 4a). On the other hand, with the initial formation of the rhizosphere (terrace 2, Fig. 4b), the contribution of lignin, tannin, and carbohydrate-like decreased by almost 50%, while that of lipid, protein and amino sugar-like compounds increased 3-fold. With increased root-driven weathering (terrace 2–5), lipid, protein, and amino sugar-like compounds decreased in their contribution. In terrace 5, the contribution of tannin, lignin, and carbohydrate-like compounds dominated rhizosphere soil, making up to ~60% of all mass peaks. In sum, non-rhizosphere and rhizosphere soil showed notably different patterns for the relative abundance of compound classes that can be attributed to plant material (e.g., lignin, tannins, and carbohydrates) and those that may be microbially-derived (e.g., lipids, proteins, and amino sugars).

3.4. Micron-scale visualization of mineral-organic associations

3.4.1. Spatial distribution of C, Fe and Al

Elemental maps recorded by STXM revealed differences in the micron-scale distribution of C, Fe, and Al between non-rhizosphere and rhizosphere soil (Fig. 5). Fig. 5a-g shows normalized false-color overlays of C, Fe, and Al

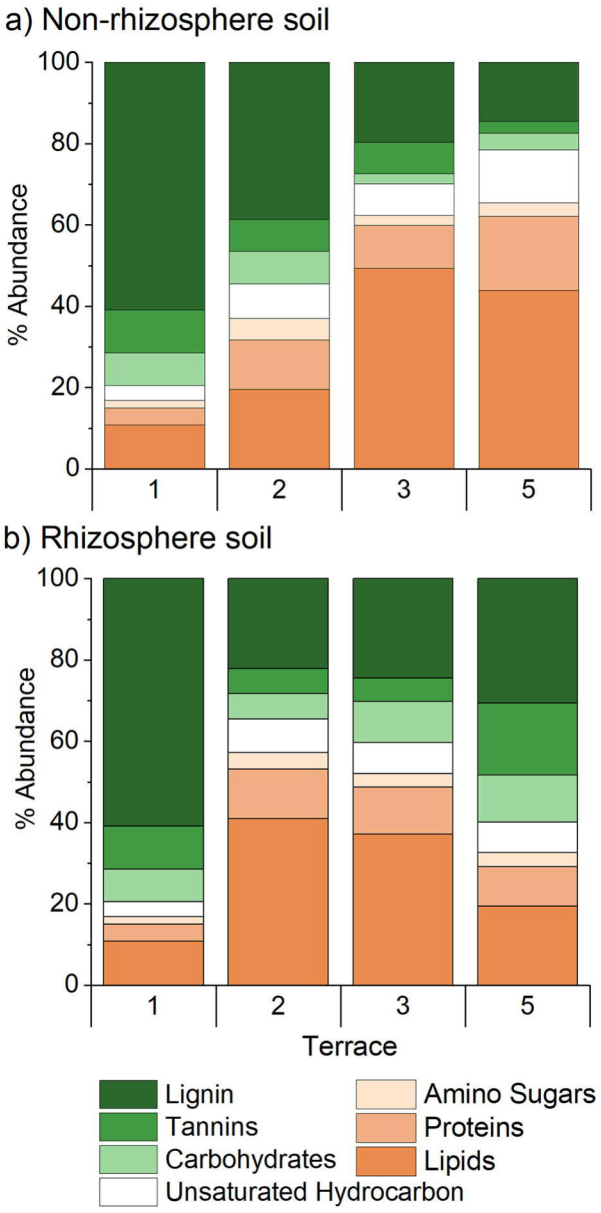

Fig. 4. Changes in abundance of different organic compound classes in water-extractable organic carbon fraction (a) non-rhizosphere and (b) rhizosphere soil across the chronosequence as determined by FT-ICR-MS. Classes given in green colors (tannins, lignin, and carbohydrates) are attributed to plant-derived compounds, those given in brown colors compounds (amino sugars, proteins, lipids, and unsaturated hydrocarbons) are assigned to microbially-derived.

maps of clay-sized particles. In terrace 1 (Fig. 5a), we observed larger (<5μm), discrete Al-rich particles as well as smaller (<1μm), Fe- and C-containing particles. In non-rhizosphere soil, discrete Fe-rich particles dominated, the abundance of which gradually increased from terrace 2 to 5 (Fig. 5b-d). When present, C-rich spots were only found in association with these discrete Fe particles (Fig. 5-b-d). Concurrently, the abundance of Al-rich particles declined. Images of rhizosphere soil contained visibly more C than non-rhizosphere soil (Fig. 5e-g). This was most notable in terrace 2, where C was distributed in a dense network of C-rich, amorphous structures. These structures, reminiscent of macromolecular aggregates observed by Myneni et al. (1999), contained small (<1 μm), dispersed Fe-rich particles (Fig. 5e). Such amorphous, C-rich structures were not visible in terraces 3 and 5 (Fig. 5f and g). Here, C-rich spots appeared more concentrated and increasingly co-localized with larger (>1 μm) Fe- and Al-rich particles. The small and dispersed Fe-rich particles were much less prominent in terraces 3 and 5 (Fig. 5f and g).

3.4.2. Quantitative image analysis

In addition to the qualitative image analysis presented above, we quantified how root-driven weathering altered the degree to which C is associated with Fe by subjecting our Fe and C maps ($n = 3$) to correlation (Fig. 5h) and colocalization analyses (Fig. 5i). We focused our imaging analysis on Fe (as opposed to Al) due to the higher spatial resolution images that can be achieved at the Fe L-edge (see methods section for detailed explanation). From terrace 1 to terrace 2, the Fe and C distributions became significantly less correlated in non-rhizosphere soil, as evidenced by declining r values from ~0.63 to ~0.30 (Fig. 5h). The r value remained low and did not change significantly thereafter. In contrast, the distribution of Fe and C in rhizosphere soil became more strongly correlated with the onset of weathering. Between terrace 1 and 2, the r value increased from 0.63 to ~0.83, a value significantly greater than that in non-rhizosphere soil ($p < 0.05$, Fisher's LSD). With continued weathering (terrace 2 to 5), r values declined gradually and significantly, approaching those in non-rhizosphere soils ($r = \sim 0.34$).

Our colocalization analysis showed analogous trends for the fraction of C that is co-localized with Fe (Fig. 5i). The amount of C associated with Fe in non-rhizosphere soil did not change significantly across the age gradient and remained between 40–50%. In contrast, the proportion of C co-located with Fe in rhizosphere soil increased to 80% in terrace 2, a value significantly greater than that found in the non-rhizosphere soil ($p < 0.05$, Fisher LSD). Between terrace 2 and 5, the amount of C co-localization with Fe gradually declined towards values observed in non-rhizosphere soils (~45%).

Taken together, our elemental mapping revealed that the initial rhizosphere differentiation (terrace 2) coincided with the formation of Fe-C associations, where small Fe oxide particles appeared to be embedded within a matrix of amorphous organic matter (Fig. 5e). As weathering in rhizosphere soil continued, larger Fe oxide particles increasingly dominated and the degree of association with C declined (Fig. 5e-f). In contrast, non-rhizosphere soils displayed consistently low amounts of C associated with Fe across the age gradient (Fig. 5b-d).

4. DISCUSSION

More than 50% of soil C is found in soils deeper than 1 m and protected within MOAs (Rumpel and Kögel-

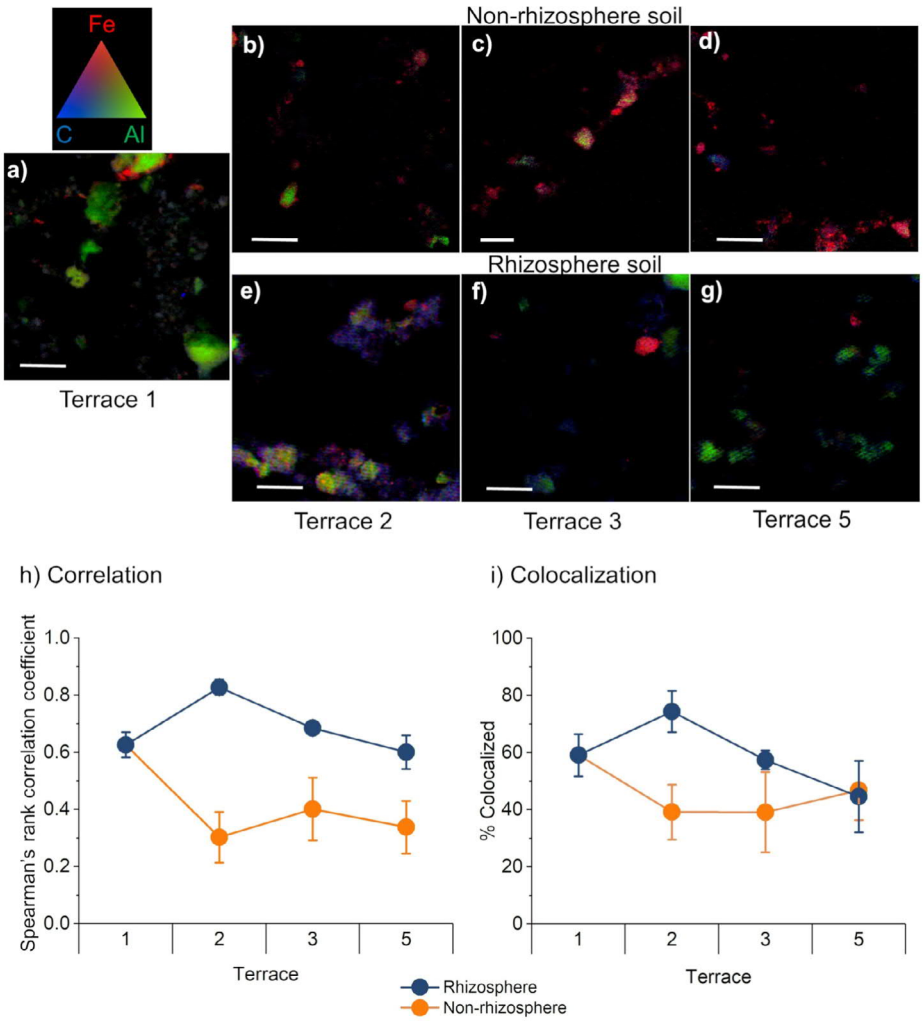

Fig. 5. Changes in the micron-scale distribution of C in relation to Fe and Al phases in rhizosphere and non-rhizosphere soil across the chronosequence. To visualize the spatial distribution of C, Fe and Al, overlay maps (Red = Fe, Green = Al, Blue = C) for non-rhizosphere (b-d) and rhizosphere soil (e-g) at each terrace are presented. Scale bars are 5 μm except for non-rhizosphere terrace 2 which is 2 μm. Terrace 1 (a) has no rhizosphere differentiation, so only a map for bulk soil is shown. To quantify spatial relationships between Fe and C, we calculated Spearman's rank correlation coefficient for three replicate maps per sample. Changes in the correlation coefficient describing the association of C and Fe are shown in panel (h). To further assess the degree of association between C and Fe, a co-localization analysis was performed (see methods for details) on three replicate images. Changes in the percentage of C associated with Fe across the chronosequence are shown in panel (i). For each analysis, bars represent standard error of the mean of three replicate images. Note that rhizosphere soil has not been established in terrace 1 and, thus, only data for bulk (i.e., non-rhizosphere soil) is reported. (For interpretation of the references to colour in this figure legend, the reader is referred to the web version of this article.)

Knabner, 2011). Although the effects of root activity on deep soil C dynamics have received increased attention (Yu et al., 2017; Poirier et al., 2018), the impact of root-driven weathering on MOAs and C storage over pedogenic time scales have yet to be understood. Our comparison of rhizosphere and non-rhizosphere soil across the Santa Cruz marine terrace chronosequence highlights the significant impact of root activity on the evolution of mineral composition, C chemistry and, consequently, the nature of MOAs during soil development. While we cannot exclude that root activity may have varied throughout time, the observed MOA dynamics are consistent with those in other chronosequence studies (Torn et al., 1997; Chorover et al., 2004; Mikutta et al., 2009), indicating that these patterns are independent of local climate or vegetation factors.

4.1. Root-driven weathering effects on quantity, age, and composition of soil carbon

Continuous root C inputs such as dead root tissue, border cells, mucilage, or exudates promote root-driven weathering over pedogenic time scales (Fimmen et al., 2008; Schulz et al., 2016). Our results show that root colonization significantly changed the C concentration (Fig. 1a), $\Delta^{14}C$

values (Fig. 1b), and chemistry (Fig. 3b) in soil directly impacted by root-driven weathering. Across the age gradient, rhizosphere soil contained more C than non-rhizosphere soil (Fig. 1a), which is consistent with previous observations of root-promoted C accumulation in deep soil (Richter et al., 1999; Fimmen et al., 2008). C accumulation became particularly significant in terrace 2, where direct root-driven weathering effects were first observable, with C concentrations in non-rhizosphere soil only half of those found in rhizosphere soil (Fig. 1a). C accumulation at terrace 2, coincided with a steep decline in both non-rhizosphere and rhizosphere soil $\Delta^{14}C$ values (Fig. 1b), suggesting longer C residence times, and a significant increase in the relative abundance of organic compounds that can be attributed to microbial sources (e.g., lipids, amino sugars, and proteins) (Fig. 4b).

The dynamics of C content and $\Delta^{14}C$ values reflect those observed for bulk soil in comparable chronosequences, which generally show an increase in C concentration and potential residence times during initial weathering stages and a decline thereafter (Torn et al., 1997; Chorover et al., 2004; Masiello et al., 2004; Mikutta et al., 2009; Lawrence et al., 2015). The increase in water-extractable, microbially-derived products during initial weathering stages and their subsequent decline in late stages follows concentrations of bacterial biomass C in bulk soils at our site (Moore et al., 2010). Fimmen et al. (2008) also noted increased microbial biomass in response to root driven-weathering, suggesting that this increase in microbially-derived C may stem from root-associated microbes. Our results thus suggest that root activity during initial root-driven weathering promoted C accumulation by triggering microbial biomass growth in the rhizosphere.

The C dynamics in non-rhizosphere soil are in sharp contrast to that in rhizosphere soil, and those observed in the aforementioned chronosequences (Torn et al., 1997; Chorover et al., 2004; Masiello et al., 2004; Mikutta et al., 2009; Lawrence et al., 2015). C concentrations gradually declined with soil age (Fig. 1a), paralleled by a gradual shift from predominantly plant-derived to microbially-derived C compounds (Fig. 4a). In the absence of direct root C inputs, the gradual shift towards microbially derived compounds could be a result of long-term changes in the amount and composition of surface dissolved organic carbon (DOC) leached into deeper soil horizons (Kramer et al., 2012) or the result of continuous microbial cycling of the C available in the non-rhizosphere soil over time (Rumpel and Kögel-Knabner, 2011).

4.2. Root-driven weathering effects on mineral composition

Roots and associated microbes create an intensive weathering regime in the rhizosphere through the introduction of organic reductants, chelators, acids or protons (e.g., Hinsinger et al., 2005), which dissolve primary minerals (Brantley et al., 2011; Violante and Caporale, 2015; Yu et al., 2017) and transform secondary minerals (April and Keller, 1990; Turpault et al., 2007; Fimmen et al., 2008; Collignon et al., 2012). Our results show that these root-driven weathering reactions significantly altered the mineralogical composition across the chronosequence. While composition and abundance of phyllosilicate clays was significantly altered, changes in the poorly and more crystalline Fe and Al phases were most directly related to root-driven weathering and C dynamics.

The development of the rhizosphere coincided with an increase in poorly crystalline phases (3-fold) (Fig. 2b), which was mirrored by the appearance of highly disordered np-goethite (Fig. 3b). At terrace 2, the most disordered np-goethite phases (type 4) represented more than 50% of all Fe oxides present. Disorder arises from substitution of Fe with Al and co-precipitation with C (Chen et al., 2015), forming smaller and more disordered np-goethite (Cornell and Schwertmann, 2003). The greater abundance of highly disordered Fe and Al phases during initial weathering stages in rhizosphere soils is consistent with the accumulation of Al and Fe hydroxides (e.g., ferrihydrite, imogolite, and allophane) observed in younger soils of comparable chronosequences (Torn et al., 1997; Chorover et al., 2004; Masiello et al., 2004; Mikutta et al., 2009). However, we did not find this trend of increasing Al and Fe hydroxides in bulk soil across the chronosequence (C. Lawrence, written communication, May 2019). This discrepancy strongly suggests that the dynamics of poorly crystalline phases are directly related to root-driven weathering.

With continued root-driven weathering the abundance of these poorly crystalline minerals decreased from terraces 2 to 5. During these later weathering stages, the contribution of crystalline Fe and Al phases increased (Fig. 3b) and shifted from highly disordered (type 4) to more ordered np-goethite (types 1–3) (Fig. 3b). This transformation from small, poorly crystalline to larger, thermodynamically stable crystalline minerals through continued weathering in rhizosphere soils is consistent with observations in more weathered soils of other chronosequences (Torn et al., 1997; Chadwick and Chorover, 2001; Masiello et al., 2004; Chorover et al., 2004). In our case, transformation (or "aging") of highly disordered np-goethite into more ordered, crystalline phases may be due to repeated redox cycles (Thompson et al., 2006), as induced by root activity (Fimmen et al., 2008). Hence, our results indicate that with recurring root colonization of rhizosphere soil over pedogenic time scales, more ordered and, thus, thermodynamically more stable Fe phases have been created.

Mineral composition and transformations in non-rhizosphere soil were distinctly different from that in rhizosphere soil across the chronosequence. Non-rhizosphere soil showed significantly lower concentrations of poorly crystalline Fe and Al phases than rhizosphere soil, with no significant changes in concentration along the soil age gradient (Fig. 2a). However, sequential extractions indicated an increase in the amount of crystalline Fe and Al with time (Fig. 2b), which is consistent with the dominance of the most ordered np-goethite phases (types 1–2) in late weathering stages (Fig. 3a). The relatively low abundance of poorly crystalline materials and slow transformation of crystalline Fe and Al phases indicate lower weathering rates, which we attribute to the lack of root C inputs and associated microbial activity.

4.3. Evolution of mineral-organic associations in rhizosphere soil

Root impacts on organic matter and mineral composition during initial and late weathering stages resulted in dramatic transformations of MOAs across the chronosequence. Initial root-driven weathering (terrace 2) coincided with a sharp increase in the amount of C associated with poorly crystalline Fe and Al phases (Fig. 2a) and was accompanied by significant increases in C accumulation and potential C residence times (Fig. 1b), highlighting the importance of such MOAs for C storage in these soil systems (Masiello et al., 2004; Lawrence et al., 2015).

The importance of the interaction of organic compounds with poorly crystalline Fe and Al phases in controlling C storage during initial root-driven weathering stages was further supported by STXM images, which showed the strongest spatial associations between Fe and C in terrace 2 (Fig. 5h and i). Fe-C associations at this weathering stage show a unique morphology, with sub-micron sized Fe minerals embedded within a matrix of amorphous C (Fig. 5e). The observation of small Fe particles closely associated with C (Fig. 5e) is consistent with our Mössbauer results, which revealed the formation of highly disordered np-goethite phases substituted with Al and/or C (Fig. 3b) at this stage. These amorphous C structures embedded within agglomerations of Fe particles are like those of macromolecular organic matter aggregates documented using high-resolution imaging elsewhere (Myneni et al., 1999; Thompson et al., 2006), suggesting a degree of microbial processing. Our mass spectrometry results (Fig. 4b) further support this notion, showing a sharp increase in the contribution of FTICRMS-detectable, potentially microbially-derived organic compounds such as amino sugars, proteins and lipids (from 20 to 80%), with the onset of root-driven weathering. Strong affinities between poorly crystalline minerals and microbially-derived compounds are in good agreement with reports by Mikutta et al. (2009), who showed that the presence of aliphatic and amide C, which are indicative of microbial residues, is highly correlated with the abundance of poorly crystalline Fe phases.

Continued root-driven weathering (terrace 3–5) resulted in the gradual loss of associations between poorly crystalline phases and microbially-derived C. STXM imaging revealed that the degree of micron-scale association of C and Fe steadily decreased during late weathering stages (Fig. 5a, e-g). This decrease in the amount of C associated with poorly crystalline Fe and Al phases (Fig. 2a) was paralleled by a decline in the contribution of highly disordered, potentially C-substituted, np-goethite phases (Fig. 3b) and microbially-derived compounds (Fig. 4b). We attribute these observations of root-induced disruption of MOAs, possibly via ligand-promoted (Keiluweit et al., 2015; Clarholm et al., 2015) or reductive dissolution (Fimmen et al., 2007). Past studies have shown that root exudates can mobilize previously Fe- and Al-associated C, enhancing its bioavailability and so causing C loss through microbial mineralization (Keiluweit et al., 2015). Similarly, Rasmussen and co-workers (Rasmussen et al., 2007; Finley et al., 2018) found that C loss in response to the addition of root exudates was most pronounced in soils with the greatest contents of poorly crystalline phases, suggesting that MOAs consisting of poorly crystalline Fe and Al are the most susceptible to root impacts. The fact that root-induced disruption of poorly crystalline Fe and Al phases in later weathering stages (terrace 3–5) coincided with a decline in C concentrations and increase in $\Delta^{14}C$ (Fig. 1) suggests that older, microbially-derived C previously-protected in such MOAs (terrace 2) was lost to microbial decomposition and/or leaching.

Although the amount of C stored in association with poorly crystalline phases diminished in late weathering stages, the fraction of C associated with crystalline Al and Fe phases remained relatively constant (Fig. 2b). At the same time, highly disordered np-goethite was gradually replaced by more ordered phases (Fig. 3b). Because the increasing order in np-goethite phases suggests a lower degree of substitution, less C may be protected within these structures. This notion is confirmed by our STXM imaging results, which show larger Al- and Fe-rich particles with only trace amounts of C (Fig. 5f-g). These findings demonstrate that MOAs dominating the later weathering stages consist of discrete, crystalline Fe and Al particles with surface coatings of organic compounds, similar to those reported by Chorover and Chadwick (2001) in highly weathered soils. Combined, our results suggest that as continued weathering disrupts highly protective MOAs between C and poorly crystalline Fe and Al phases, less protective MOAs between C and more stable, crystalline phases are left behind.

4.4. Evolution of mineral-organic associations in non-rhizosphere soil

In contrast to the dramatic change in nature of MOAs in rhizosphere soil, MOAs in non-rhizosphere soil showed no or only gradual transformations and, consequently, lower C accumulation. In fact, the amount of C associated with poorly crystalline phases, which was significantly lower than that in rhizosphere soil, steadily decreased with soil age (Fig. 2a). This decrease in C associated with poorly crystalline phases was accompanied by a gradual decline in C concentrations (Fig. 1a). These findings suggest that root activity and associated weathering is necessary to form poorly crystalline minerals and supply C compounds for the formation of MOAs, which could provide a mechanism for C accumulation in deep soils. In the absence of roots, as observed in the non-rhizosphere soil here, weathering driven by surface-derived DOC alone (e.g., Kramer et al., 2012) does not seem to generate significant amounts of protective MOAs and, thus, fails to accumulate C at the same rate.

Compared to rhizosphere soil, a significantly larger fraction of C in the non-rhizosphere soil was associated with crystalline Fe and Al phases (Fig. 2). Nevertheless, the total amount of C associated with these phases is low, consistent with the low degree of micron-scale association between Fe and C at the sub-micron scale as evidenced by STXM (Fig. 5h-i). Carbon, if present, was found in association

with large discrete Fe and Al particles across the chronosequence (Fig. 5e-g). These findings imply that Fe and Al phases with greater crystallinity might have lower C loadings and, consequently, have a lower capacity to protect MOA from microbial decomposition. Overall, our results suggest that non-rhizosphere soils store less C than rhizosphere soils due to the lack of poorly crystalline phases and the relative dominance of highly crystalline Fe and Al phases with low C loadings.

4.5. Root-driven weathering generates and disrupts protective mineral-organic associations

Our comparison of rhizosphere and non-rhizosphere soil demonstrate that roots are important agents of formation, transformation, and disruption of MOAs over pedogenic time scales. The evolution of MOAs under the influence of root-driven weathering at our site is conceptualized in Fig. 6 and summarized as follows: Terrace 1 represents ini-

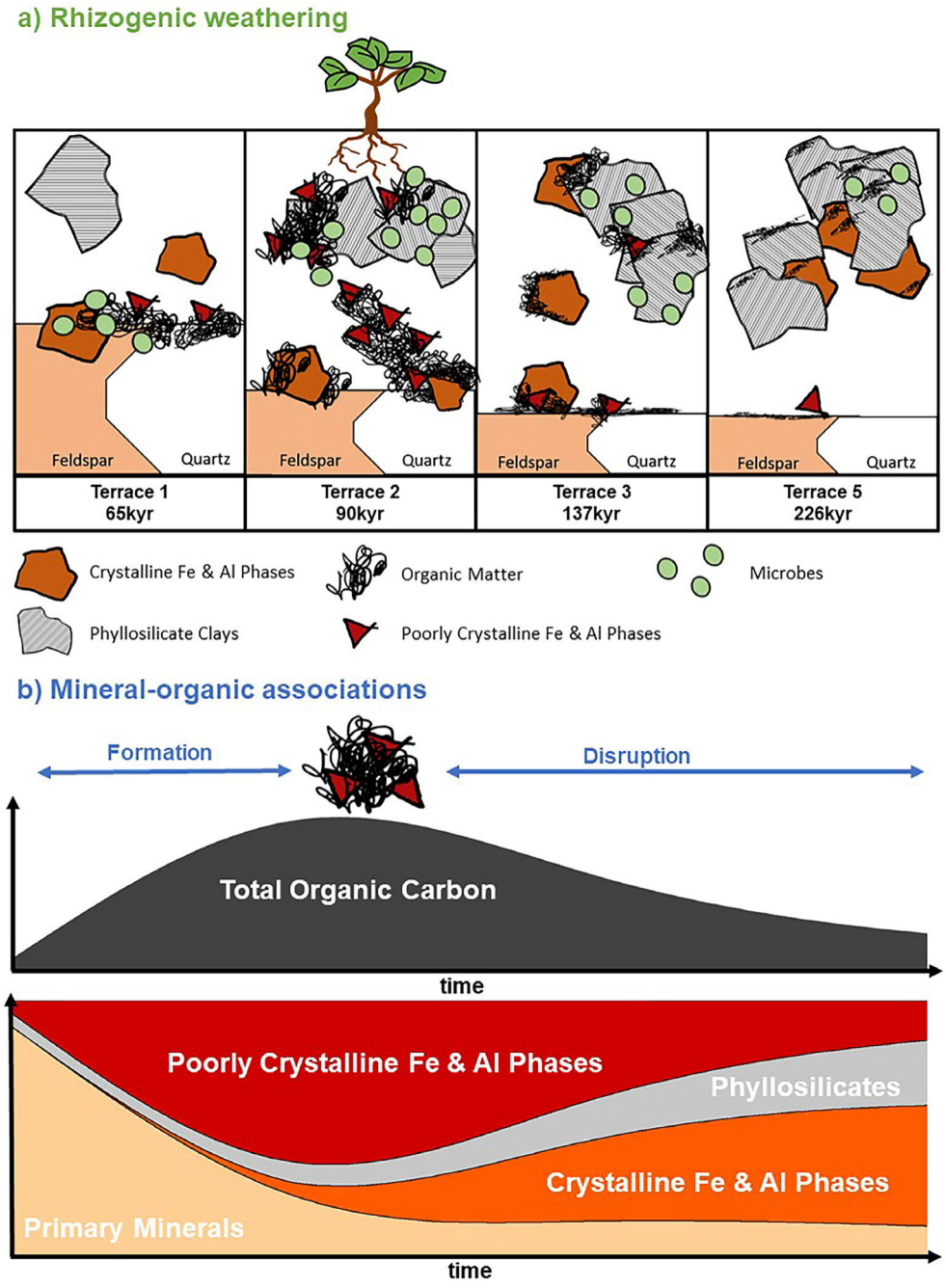

Fig. 6. Proposed model for root-driven weathering impacts on mineral-organic associations and their impact on soil C storage over pedogenic timescales. (a) Root-driven formation of mineral-organic associations at younger terraces 1 and 2 and root-mediated disruption of mineral-organic associations at older terraces 3 and 5. (b) Corresponding dynamics in soil C as well as primary and secondary mineral phases throughout younger and older terraces. A detailed discussion of the depicted processes can be found in the main text.

tial weathering stages prior to root colonization of deep soils. In the absence of roots, weathering of primary minerals, is mainly driven by DOC leaching and the accumulation of C in association with poorly crystalline Fe and Al phases, is slow. In terrace 2, root colonization triggers intense root-driven weathering of primary minerals (i.e., feldspar and quartz), either directly through root exudates (Richter et al., 2007; Hinsinger and Courchesne, 2008; Bonneville et al., 2011) or indirectly through changes in the geochemical regime (e.g., pH or Eh) (Fimmen et al., 2008; Schulz et al., 2016). Root-driven weathering accelerates formation of MOAs between poorly crystalline Fe and Al phases with microbially-derived organic matter, thereby driving C accumulation in the early weathering stages. In terraces 3 and 5 continual root-driven weathering disrupts associations between organic matter and poorly crystalline phases, leaving behind chemically more stable yet less protective MOAs consisting of more crystalline phases. This change in the nature and reactivity of MOAs is paralleled by C loss during later weathering stages. The dynamics in adjacent soils not directly affected by root-driven weathering (non-rhizosphere soil) were distinctly different, showing no significant generation of MOAs consisting of poorly crystalline phases. Instead, the amount of C associated with crystalline mineral phases gradually declined, corresponding to a loss of C over time.

The formation of MOAs between poorly crystalline Fe and Al phases in early weathering stages and disruption of such MOAs during later weathering stages in rhizosphere soil is consistent with observations in other chronosequence studies (Torn et al., 1997; Chorover et al., 2004; Mikutta et al., 2009). In these studies, the abundance of poorly crystalline Fe and Al phases across soils of different weathering stages was directly related to the amount of mineral-associated C, overall C stocks and residence times. However, because these studies focused on relatively shallow and/or well-homogenized bulk soils, the effect of root-driven weathering could not be isolated. Since the general temporal pattern of initial MOA formation followed by disruption with increasing soil weathering observed in other chronosequences match those observed in the rhizosphere soil examined here, but not that of our non-rhizosphere soil, we suggest that root activity is a principal, yet largely overlooked driver of MOA dynamics during soil formation.

4.6. Implications for the vulnerability of deep soil carbon to root-driven weathering impacts

Anthropogenic and environmental drivers such as increasing atmospheric CO_2 levels (Kuzyakov 2011), land use change (Richter et al., 1999), nutrient depletion (Husson, 2013), or drought (Schenk, 2008) are thought to increase root growth into deeper soil horizons. But whether enhanced root activity in deep soil will enhance C storage at depth or deplete old C stored in MOAs remains a topic of debate (Richter et al., 1999; Fontaine et al., 2007; Hicks-Pries et al., 2017). Our results are in accordance with past studies that suggest the impact of root growth in deep soils depends on the developmental stage and mineralogical composition of the soil. Here we find that enhanced root activity in relatively young soils may lead to C accrual through formation of new MOAs. Conversely, increased root colonization of older, more weathered soil may disrupt existing MOAs and cause the loss of C protected therein. These insights may therefore be useful in distinguishing soils that lend themselves to root-promoted C storage at depth and those that would be vulnerable to root-induced soil C loss.

Although roots are now recognized as the predominant source of soil C in deep soils (Rumpel and Kögel-Knabner, 2011), and their physical traits are increasingly relied upon to predict soil C storage (Poirier et al., 2018), the effect of root-induced weathering has largely been overlooked. Current models reflect roots as passive conduits of C and nutrients (Dwivedi et al., 2017). While models have started to incorporate root effects on microbial activity (e.g., priming effects) (Sulman et al., 2014; Dwivedi et al., 2017), the direct impacts of root-driven weathering reactions on MOA formation and disruption are not currently considered. Our results show that the ability of root-driven weathering to both create or disrupt MOA and thereby regulate soil C storage may warrant model incorporation. Recent approaches using reactive transport models that begin to prioritize the incorporation of root-driven weathering reactions hold great promise (Lawrence et al., 2014; Li et al., 2017).

ACKNOWLEDGEMENTS

We are thankful for the detailed and thoughtful reviews by the Associate Editor J. Chorover, three anonymous reviewers, and C. Creamer, which greatly improved the quality of this paper. We would also like to thank A. Chica and H. Mashayekhi for their laboratory assistance, as well as K. Campbell and T. Kane of the U.S. Geological Survey for their help in collecting the X-ray diffraction data. MGA was supported by the National Science Foundation Graduate Research Fellowship Program. KB was supported by the SLAC SFA research program (SLAC FWP 10094), which is funded by the U.S. Department of Energy (DOE) Subsurface Biogeochemical Research (SBR) program within the Office of Biological and Environmental Research. Support for MS and CL was provided by the U.S. Geological Survey Land Change Science Program. We thank Jay Dynes and Jian Wang for their help at the SM beamline at the Canadian Light Source, which is supported by the Canada Foundation for Innovation, Natural Sciences and Engineering Research Council of Canada, the University of Saskatchewan, the Government of Saskatchewan, Western Economic Diversification Canada, the National Research Council Canada, and the Canadian Institutes of Health Research. A portion of this research was performed using EMSL, an DOE Office of Science User Facility sponsored by the Office of Biological and Environmental Research. Any use of trade, firm, or product names is for descriptive purposes only and does not imply endorsement by the U.S. Government. This work was supported by the DOE, Office of Biological and Environmental Research, SBR program (award no. DE-SC0019477).

REFERENCES

Abramoff M. D., Magalhaes P. J. and Ram S. J. (2004) Image processing with ImageJ. *Biophotonics Int.* **11**, 36–42.

April R. and Keller D. (1990) Mineralogy of the rhizosphere in forest soils of the eastern United States – Mineralogic studies of the rhizosphere. *Biogeochemistry* **9**, 1–18. https://doi.org/10.1007/BF00002714.

Augusto L., Ranger J., Turpault M.-P. and Bonnaud P. (2001) Experimental in situ transformation of vermiculites to study the weathering impact of tree species on the soil. *Eur. J. Soil Sci.* **52**, 81–92. https://doi.org/10.1046/j.1365-2389.2001.t01-1-00359.x.

Bhattacharyya A., Campbell A. N., Tfaily M. M., Lin Y., Kukkadapu R. K., Silver W. L., Nico P. S. and Pett-Ridge J. (2018) Redox fluctuations control the coupled cycling of iron and carbon in tropical forest soils. *Environ. Sci. Technol.* **24**, 14129–14139. https://doi.org/10.1021/acs.est.8b03408.

Bernal B., McKinley D. C., Hungate B. A., White P. M., Mozdzer T. J. and Megonigal J. P. (2016) Limits to soil carbon stability: deep, ancient soil carbon decomposition stimulated by new labile organic inputs. *Soil Biol. Biochem.* **98**, 85–94. https://doi.org/10.1016/j.soilbio.2016.04.007.

Bernal B., Megonigal J. P. and Mozdzer T. J. (2017) An invasive wetland grass primes deep soil carbon pools. *Glob. Change Biol.* **23**, 2104–2116. https://doi.org/10.1111/gcb.13539.

Bonneville S., Morgan D. J., Schmalenberger A., Bray A., Brown A., Banwart S. A. and Benning L. G. (2011) Tree-mycorrhiza symbiosis accelerate mineral weathering: evidences from nanometer-scale elemental fluxes at the hypha-mineral interface. *Geochim. Cosmochim. Acta* **75**, 6988–7005. https://doi.org/10.1016/j.gca.2011.08.041.

Brantley S. L., Megonigal J. P., Scatena F. N., Balogh-Brunstad Z., Barnes R. T., Bruns M. A., Van Capellen P., Dontsova K., Hartnett H. E., Hartshorn A. S., Heimsath A., Herndon E., Jin L., Keller C. K., Leake J. R., McDowell W. H., Meinzer F. C., Mozdzer T. J., Petsch S., Pett-Ridge J., Pregitzer K. S., Raymond P. A., Riebe C. S., Shumaker K., Sutton-Grier A., Walter R. and Yoo K. (2011) Twelve testable hypotheses on the geobiology of weathering. *Geobiology* **9**, 140–165. https://doi.org/10.1111/j.1472-4669.2010.00264.

Chadwick O. A. and Chorover J. (2001) The chemistry of pedogenic thresholds. *Geoderma* **100**, 321–353. https://doi.org/10.1016/S0016-7061(01)00027-1.

Chen C., Kukkadapu R. and Sparks D. L. (2015) Influence of coprecipitated organic matter on Fe2+ (aq)-catalyzed transformation of ferrihydrite: implications for carbon dynamics. *Environ. Sci. Technol.* **18**, 10927–10936. https://doi.org/10.1021/acs.est.5b02448.

Chorover J., Amistadi M. K. and Chadwick O. A. (2004) Surface charge evolution of mineral-organic complexes during pedogenesis in Hawaiian basalt. *Geochim. Cosmochim. Acta* **68**, 4859–4876. https://doi.org/10.1016/j.gca.2004.06.005.

Clarholm M., Skyllberg U. and Rosling A. (2015) Organic acid induced release of nutrients from metal-stabilized soil organic matter: the unbutton model. *Soil Biol. Biochem.* **84**, 168–176. https://doi.org/10.1016/j.soilbio.2015.02.019.

Clemmensen K. E., Bahr A., Ovaskainen O., Dahlberg A., Ekblad A., Wallander H., Stenlid J., Finlay R. D., Wardle D. A. and Lindahl B. D. (2013) Roots and associated fungi drive long-term carbon sequestration in boreal forest. *Science* **339**, 1615–1618. https://doi.org/10.1126/science.1231923.

Collignon C., Ranger J. and Turpault M. P. (2012) Seasonal dynamics of Al- and Fe-bearing secondary minerals in an acid forest soil: influence of Norway spruce roots (Picea abies (L.) Karst.). *Eur. J. Soil Sci.* **63**, 592–602. https://doi.org/10.1111/j.1365-2389.2012.01470.x.

Cook D. C., Oh S. J., Balasubramanian R. and Yamashita M. (1999) The role of goethite in the formation of the protective corrosion layer on steels. *Hyperfine Interact.* **122**, 59–70. https://doi.org/10.1023/A:1012685320582.

Cornell R. M. and Schwertmann U. (2003) *The Iron Oxides*. Wiley-VCH GmbH & Co. KGaA, Weinheim, https://doi.org/10.1002/3527602097.

Dwivedi D., Riley W., Torn M., Spycher N., Maggi F. and Tang J. (2017) Mineral properties, microbes, transport, and plant-input profiles control vertical distribution and age of soil carbon stocks. *Soil Biol. Biochem.* **107**, 244–259. https://doi.org/10.1016/j.soilbio.2016.12.019.

Eberl D. D. (2003) User guide to RockJock – A program for determining quantitative mineralogy from X-ray diffraction data, U.S. Geological Survey Open-File Report, 2003-78.

El-Sabbagh D. and Garrison R. E. (1990) Silica digenesis in the Santa Cruz Mudstone (upper Miocene), La Honda Basin, California. In Geology and Tectonics of the Central California Coast Region, San Francisco to Monterey, pp. 123–132.

Ewing S. A., Sanderman J., Baisden W. T., Wang Y. and Amundson R. (2006) Role of large-scale soil structure in organic carbon turnover: evidence from California grassland soils. *J. Geophys. Res.* **111**. https://doi.org/10.1029/2006JG000174.

Fan Y., Miguez-Macho G., Jobbágy E. G., Jackson R. B. and Otero-Casal C. (2017) Hydrologic regulation of plant rooting depth. *Proc. Natl. Acad. Sci.* **114**, 10572–10577. https://doi.org/10.1073/pnas.1712381114.

Fimmen R. L., Richter D. B., Vasudevan D., Williams M. A. and West L. T. (2008) Rhizogenic Fe–C redox cycling: a hypothetical biogeochemical mechanism that drives crustal weathering in upland soils. *Biogeochemistry* **87**, 127–141. https://doi.org/10.1007/s10533-007-9172-5.

Finley B. K., Dijkstra P., Rasmussen C., Schwartz E., Mau R. L., Liu X.-J. A., van Gestel N. and Hungate B. A. (2018) Soil mineral assemblage and substrate quality effects on microbial priming. *Geoderma* **322**, 38–47. https://doi.org/10.1016/j.geoderma.2018.01.039.

Fischer W. R., Flessa H. and Schaller G. (1989) pH values and redox potentials in microsites of the rhizosphere. *Zeitschrift Für Pflanzenernährung Und Bodenkunde* **152**, 191–195. https://doi.org/10.1002/jpln.19891520209.

Fontaine S., Barot S., Barré P., Bdioui N., Mary B. and Rumpel C. (2007) Stability of organic carbon in deep soil layers controlled by fresh carbon supply. *Nat. Lett.* **450**, 277–280. https://doi.org/10.1038/nature06275.

Fysh S. A. and Clark P. E. (1982a) Aluminous goethite: a Mössbauer study. *Phys. Chem. Miner.* **8**, 180–187. https://doi.org/10.1007/BF00308241.

Fysh S. A. and Clark P. E. (1982b) Aluminous hematite: a Mössbauer study. *Phys. Chem. Miner.* **8**, 257–267. https://doi.org/10.1007/BF00308247.

Harper R. J. and Tibbett M. (2013) The hidden organic carbon in deep mineral soils. *Plant Soil* **368**, 641–648. https://doi.org/10.1007/s11104-013-1600-9.

Heckman K., Lawrence C. R. and Harden J. W. (2018) A sequential selective dissolution method to quantify storage and stability of organic carbon associated with Al and Fe hydroxide phases. *Geoderma* **312**, 24–35. https://doi.org/10.1016/j.geoderma.2017.09.043.

Heinemeyer A., Hartley I. P., Evans S. P., Carreira De La Fuente J. A. and Ineson P. (2007) Forest soil CO2 flux: uncovering the contribution and environmental responses of ectomycorrhizas. *Glob. Change Biol.* **13**, 1786–1797. https://doi.org/10.1111/j.1365-2486.2007.01383.x.

Hicks-Pries C. E., Castanha C., Porras R. C. and Torn M. S. (2017) The whole-soil carbon flux in response to warming. *Science* **355**, 1–9. https://doi.org/10.1126/science.aal1319.

Hinsinger P. and Courchesne F. (2008) *Biogeochemistry of metals and metalloids at the soil–root interface*. Wiley, Hoboken, USA, pp. 267–311, https://doi.org/10.1002/9780470175484.ch7.

Hinsinger P., Gobran G. R., Gregory P. J. and Wenzel W. W. (2005) Rhizosphere geometry and heterogeneity arising from root-mediated physical and chemical processes. *New Phytol.* **168**, 293–303. https://doi.org/10.1111/j.1469-8137.2005.01512.x.

Husson O. (2013) Redox potential (Eh) and pH as drivers of soil/plant/microorganism systems: a transdisciplinary overview pointing to integrative opportunities for agronomy. *Plant Soil* **362**, 389–417. https://doi.org/10.1007/s11104-012-1429-7.

Jobbagy E. G. and Jackson R. B. (2000) The vertical distribution of soil organic carbon and its relation to climate and vegetation. *Ecol. Appl.* **10**, 423–436. https://doi.org/10.1890/1051-0761(2000) 010[0423:TVDOSO]2.0.CO;2.

Jung A. V., Chanudet V., Lartiges B. S., Ghanbaja J., Abdelmoula M. and Bersillon J. L. (2012) Association of iron oligomeric species with natural organic matter: a combined EELS and Mössbauer investigation. *Aquat. Sci.* **74**, 769. https://doi.org/10.1007/s00027-012-0260-9.

Kaplan D. I., Kukkadapu R. K., Seaman J. C., Arey B. W., Dohnalkova A., Buettner S., Li D., Varga T., Scheckel G. and Jaffe P. R. (2016) Iron mineralogy and uranium-binding in the rhizosphere of a wetland soil. *Sci. Total Environ.* **569–570**, 53–64. https://doi.org/10.1016/j.scitotenv.2016.06.120.

Keiluweit M., Bougoure J. J., Nico P. S., Pett-Ridge J., Weber P. K. and Kleber M. (2015) Mineral protection of soil carbon counteracted by root exudates. *Nat. Climate Change* **5**, 588–595. https://doi.org/10.1038/NCLIMATE2580.

Kim S., Kramer R. W. and Hatcher P. G. (2003) Graphical method for analysis of ultrahigh-resolution broadband mass spectra of natural organic matter, the van Krevelen diagram. *Anal. Chem.* **75**, 5336–5344. https://doi.org/10.1021/ac034415p.

Kleber M., Eusterhues K., Keiluweit M., Mikutta C., Mikutta R. and Nico P. S. (2015) Mineral–organic associations: formation, properties, and relevance in soil environments. In Advances in Agronomy (ed. D. L. Sparks). vol. 130, pp. 1–140. Available at: https://doi.org/10.1016/S0065-2113(15)00034-6.

Kramer M. G., Sanderman J., Chadwick O. A., Chorover J. and Vitousek P. M. (2012) Long-term carbon storage through retention of dissolved aromatic acids by reactive particles in soil. *Glob. Change Biol.* **18**, 2594–2605. https://doi.org/10.1111/j.1365-2486.2012.02681.x.

Kuzyakov Y. (2011) Ecology: prime time for microbes. *Nat. Clim. Change* **1**, 295–297. https://doi.org/10.1038/nclimate1194.

Lawrence C. R., Harden J. W., Xu X., Schulz M. S. and Trumbore S. E. (2015) Long-term controls on soil organic carbon with depth and time: a case study from the Cowlitz River Chronosequence, WA USA. *Geoderma* **94**, 91–107. https://doi.org/10.1016/j.geoderma.2015.02.005.

Lawrence C., Harden J. and Maher K. (2014) Modeling the influence of organic acids on soil weathering. *Geochem. Cosmochim. Acta* **139**, 487–507. https://doi.org/10.1016/j.gca.2014.05.003.

Leake J. R., Duran A. L., Hardy K. E., Johnson I., Beerling D. J., Banwart S. A. and Smits M. (2008) Biological weathering in soil: the role of symbiotic root-associated fungi biosensing minerals and directing photosynthate-energy into grain-scale mineral weathering. *Mineral. Mag.* **72**, 85–89. https://doi.org/10.1180/minmag.2008.072.1.85.

Li L., Maher K., Navarre-Sitchler A., Druhan J., Meile C., Lawrence C., Moore J., Perdrial J., Sullivan P., Thompson A., Jin C. I., Bolton E. W., Brantley S. L., Dietrich W. E., Mayer K. U., Steefel C. I., Valocchi A., Zachara J., Kocar B., Mcintosh J., Tutolo B. M., Kumar M., Sonnenthal E., Bao C. and Beisman J. (2017) Expanding the role of reactive transport models in critical zone processes. *Earth Sci. Rev.* **165**, 280–301. https://doi.org/10.1016/J.EARSCIREV.2016.09.001.

Maher K., Steefel C. I., White A. F., Stonestrom D. A. and Maher K. (2009) The role of reaction affinity and secondary minerals in regulating chemical weathering rates at the Santa Cruz soil chronosequence, California. *Geochim. Cosmochim. Acta* **73**, 2804–2831. https://doi.org/10.1016/j.gca.2009.01.030.

Masiello C. A., Chadwick O. A., Southon J., Torn M. S. and Harden J. W. (2004) Weathering controls on mechanisms of carbon storage in grassland soils. *Global Biogeochem. Cycles* **18**, 1–9. https://doi.org/10.1029/2004GB002219.

Mikutta R., Schaumann G. E., Gildemeister D., Bonneville S., Kramer M. G., Chorover J., Chadwick O. A. and Guggenberger G. (2009) Biogeochemistry of mineral-organic associations across a long-term mineralogical soil gradient (0.3-4100 kyr), Hawaiian Islands. *Geochim. Cosmochim. Acta* **73**, 2034–2060. https://doi.org/10.1016/j.gca.2008.12.028.

Moore J., Macalady J. L., Schulz M. S., White A. F. and Brantley S. L. (2010) Shifting microbial community structure across a marine terrace grassland chronosequence, Santa Cruz, California. *Soil Biol. Biochem.* **42**, 21–31. https://doi.org/10.1016/j.soilbio.2009.09.015.

Myneni S. C. B., Brown J. T., Martinez G. A. and Meyer-Ilse W. (1999) Imaging of humic substance macromolecular structures in water and soils. *Science* **286**, 1335–1337. https://doi.org/10.1126/science.286.5443.1335.

Oh N. H. and Richter D. (2005) Elemental translocation and loss from three highly weathered soil-bedrock profiles in the Southeastern United States. *Geoderma* **126**, 5–25. https://doi.org/10.1016/j.geoderma.2004.11.005.

Peretyazhko T. S., J. M., Z., Kukkadapu R. K., Heald S. M., Kutnyakov I. V., Resch C. T., Arey B. W., Wang C. M., Kovarik L., Philips J. L. and Moore D. A. (2013) Pertechnetate (TcO4-) reduction by reactive ferrous iron forms in naturally anoxic, redox transition zone sediments from the hanford site. *Geochem. Cosmochim. Acta* **92**, 48–66. https://doi.org/10.1016/j.gca.2012.05.041.

Perg L. A., Anderson R. S. and Finkel R. C. (2001) Use of a new ^{10}Be and ^{26}Al inventory method to date marine terraces, Santa Cruz, California, USA. *Geology* **29**, 879. https://doi.org/10.1130/0091-7613(2001) 029<0879:UOANBA>2.0.CO;2.

Poirier V., Roumet C. and Munson A. D. (2018) The root of the matter: linking root traits and soil organic matter stabilization processes. *Soil Biol. Biochem.* **120**, 246–259. https://doi.org/10.1016/j.soilbio.2018.02.016.

Rancourt D. G. and Ping J. Y. (1991) Voigt-based methods for arbitrary-shape static hyperfine parameter distributions in Mössbauer spectroscopy. *Nucl. Instrum. Methods Phys. Res., Sect. B* **58**, 85–97. https://doi.org/10.1016/0168-583X(91)95681-3.

Rasmussen C., Southard R. J. and Horwath W. R. (2007) Soil mineralogy affects conifer forest soil carbon source utilization and microbial priming. *Soil Sci. Soc. Am. J.* **71**, 1141. https://doi.org/10.2136/sssaj2006.0375f.

Richter D. D., Markewitz D., Trumbore S. E. and Wells C. G. (1999) Rapid accumulation and turnover of soil carbon in a re-establishing forest Present understanding of the global carbon cycle is limited by uncertainty over soil-carbon dynamics. *Nature* **400**. https://doi.org/10.1038/21867.

Richter D. D., Oh N.-H., Fimmen R. and Jackson J. (2007) The rhizosphere and soil formation. In *The Rhizosphere: An Ecological Perspective*. Academic Press, Amsterdam, pp. 179–200. https://doi.org/10.1016/B978-012088775-0/50010-0.

Ross G. J. and Wang C. (1993) Extractable Al, Fe, Mn, and Si, In soil sampling and methods of analysis. In *Canadian Society of Soil Science* (ed. M. R. Carter). Lewis Publishers, Boca Raton, FL, pp. 239–246.

Rueden C. T., Schindelin J., Hiner M. C., DeZonia B. E., Walter A. E., Arena E. T. and Eliceiri K. W. (2017) Image J2: ImageJ for the next generation of scientific image data. *BMC Bioinf.* **18**, 529. https://doi.org/10.1186/s12859-017-1934-z.

Rumpel C. and Kögel-Knabner I. (2011) Deep soil organic matter—a key but poorly understood component of terrestrial C cycle. *Plant Soil* **338**, 143–158. https://doi.org/10.1007/s11104-010-0391-5.

Schenk H. J. and Jackson R. B. (2002) The global biogeography of roots. *Ecol. Monogr.* **72**, 311–328. https://doi.org/10.1890/0012-9615(2002)072[0311:TGBOR]2.0.CO;2.

Schenk H. J. (2008) Soil depth, plant rooting strategies and species' niches. *New Phytol.* **178**, 223–225. https://doi.org/10.1111/j.1469-8137.2008.02427.x.

Schindelin J., Arganda-Carreras I., Frise E., Kaynig V., Longair M., Pietzsch T., Preibisch S., Rueden C., Saalfeld S., Schmid B., Tinevez J.-Y., White D. J., Hartenstein V., Eliceiri K., Tomancak P. and Cordona A. (2012) Fiji: an open-source platform for biological-image analysis. *Nat. Methods* **9**, 676–682. https://doi.org/10.1038/nmeth.2019.

Schulz M., Lawrence C., Muhs D., Prentice C. and Flanagan S. (2018) Landscapes from the waves—Marine terraces of California. *U.S. Geological Survey Fact Sheet*, 2018–3002. https://doi.org/10.3133/fs20183002.

Schulz M., Stonestrom D., Lawrence C., Bullen T., Fitzpatrick J., Kyker-Snowman E., Manning J. and Mnich M. (2016) Structured heterogeneity in a marine terrace chronosequence: upland mottling. *Vadose Zone J.* **15**. https://doi.org/10.2136/vzj2015.07.0102.

Seguin V., Courschesne F., Gagnon C. and Martin R. R. (2005) Mineral weathering in the rhizosphere of forested soils. In *Biogeochemistry of Trace Elements in the Rhizosphere* (eds. P. M. Huang and G. R. Gobran). Elsevier, pp. 29–55. https://doi.org/10.1016/B978-044451997-9/50004-0.

Sulman B. N., Phillips R. P., Oishi A. C., Shevliakova E. and Pacala S. W. (2014) Microbe-driven turnover offsets mineral-mediated storage of soil carbon under elevated CO2 The sensitivity of soil organic carbon (SOC) to changing environmental conditions represents a critical uncertainty in coupled carbon cycle–climate models. *Nat. Climate* **4**, 1099–1102. https://doi.org/10.1038/NCLIMATE2436.

Tarnocai C., Canadell J. G., Schuur E. A. G., Kuhry P., Mazhitova G. and Zimov S. (2009) Soil organic carbon pools in the northern circumpolar permafrost region. *Global Biogeochem. Cycles* **23**. https://doi.org/10.1029/2008GB003327.

Tfaily M. M., Chu R. K., Tolić N., Roscioli K. M., Anderton C. R., Paša-Tolić L., Robinson E. W. and Hess N. J. (2015) Advanced solvent based methods for molecular characterization of soil organic matter by high-resolution mass spectrometry. *Anal. Chem.* **87**, 5206–5215. https://doi.org/10.1021/acs.analchem.5b00116.

Thompson A., Chadwick O. A., Boman S. and Chorover J. (2006) Colloid mobilization during soil iron redox oscillations. *Environ. Sci. Technol.* **40**, 5743–5749. https://doi.org/10.1021/es061203b.

Tolić N., Liu Y., Liyu A. V., Shen Y., Tfaily M. M., Kujawinski E. B., Longnecker K., Kuo L. J., Robinson E. W., Paša-Tolić L. and Hess N. J. (2017) Formularity: software for automated formula assignment of natural and other organic matter from ultra-high resolution mass spectra PNNL-SA-128094. *Anal. Chem.* **89**, 12659–12665. https://doi.org/10.1021/acs.analchem.7b03318.

Torn M. S., Trumbore S. E., Chadwick O. A., Vitousek P. M. and Hendricks D. M. (1997) Mineral control of soil organic carbon storage and turnover. *Nature* **389**, 170–173. https://doi.org/10.1038/38260.

Turpault M.-P., Gobran G. R. and Bonnaud P. (2007) Temporal variations of rhizosphere and bulk soil chemistry in a Douglas fir stand. *Geoderma* **137**, 490–496. https://doi.org/10.1016/J.GEODERMA.2006.10.005.

Violante A. and Caporale A. G. (2015) Biogeochemical processes at soil-root interface. *J. Soil Sci. Plant Nutr.* **15**, 422–448. https://doi.org/10.4067/S0718-95162015005000038.

Wagai R. and Mayer L. M. (2007) Sorptive stabilization of organic matter in soils by hydrous iron oxides. *Geochim. Cosmochim. Acta* **71**, 25–35. https://doi.org/10.1016/j.gca.2006.08.047.

White A. F., Schulz M. S., Vivit D. V., Blum A. E., Stonestrom D. A. and Anderson S. P. (2008) Chemical weathering of a marine terrace chronosequence, Santa Cruz, California I: interpreting rates and controls based on soil concentration–depth profiles. *Geochim. Cosmochim. Acta* **72**, 36–68. https://doi.org/10.1016/j.gca.2007.08.029.

White A. F., Schulz M. S., Stonestrom D. A., Vivit D. V., Fitzpatrick J., Bullen T. D., Maher K. and Blum A. E. (2009) Chemical weathering of a marine terrace chronosequence, Santa Cruz, California. Part II: solute profiles, gradients and the comparisons of contemporary and long-term weathering rates. *Geochim. Cosmochim. Acta* **73**, 2769–2803. https://doi.org/10.1016/j.gca.2009.01.029.

White A. F., Schulz M. S., Vivit D. V., Bullen T. D. and Fitzpatrick J. (2012) The impact of biotic/abiotic interfaces in mineral nutrient cycling: a study of soils of the Santa Cruz chronosequence, California. *Geochim. Cosmochim. Acta* **77**, 62–85. https://doi.org/10.1016/j.gca.2011.10.029.

White R. G. and Kirkegaard J. A. (2010) The distribution and abundance of wheat roots in a dense, structured subsoil – implications for water uptake. *Plant, Cell Environ.* **33**, 133–148. https://doi.org/10.1111/j.1365-3040.2009.02059.x.

Xu X., Trumbore S. E., Zheng S., Southon J. R., McDuffee K. E., Luttgen M. and Liu J. C. (2007) Modifying a sealed tube zinc reduction method for preparation of AMS graphite targets: reducing background and attaining high precision. *Nucl. Instrum. Methods Phys. Res. Section B-Beam Interactions Mater. Atoms* **259**, 320–329. https://doi.org/10.1016/j.nimb.2007.01.175.

Yu G., Xiao J., Hu S., Polizzotto M. L., Zhao F., McGrath S. P., Li H., Ran W. and Shen Q. (2017) Mineral availability as a key regulator of soil carbon storage. *Environ. Sci. Technol.* **51**, 4960–4969. https://doi.org/10.1021/acs.est.7b00305.

Associate editor: Jon Chorover